19th Australasian Fluid Mechanics Conference
Melbourne, Australia
8-11 December 2014

Stability Characteristics of Low-Amplitude Jets in Cross-Flow

J. H. Watmuff

School of Aerospace, Mech. & Manuf. Eng.
RMIT University
Bundoora, VIC, 3083 AUSTRALIA

Abstract

The jet in cross-flow features complex fully three-dimensional dynamics that cannot be fully investigated using the simplifying assumptions commonly applied to simpler flows. The jet in cross-flow has recently been explored by the *KTH* Group using a spectral CFD code in conjunction with global stability analysis. The complex dynamics are now well understood, at least for small values of the jet-to-cross-flow velocity ratio R. This establishes the low-amplitude jet in cross-flow as a suitable test case for investigating the accuracy, capabilities and limitations of various CFD solvers. The *KTH* investigations use a simplified velocity profile with axial symmetry for the jet inflow. With some care, results with much the same stability characteristics have been obtained for this configuration using the ANSYS Fluent CFD solver. Simulations have also been conducted in which the jet fluid originates from a tube connected to the orifice. The simplified jet inflow velocity profile used in the *KTH* configuration is shown to be physically unrealistic. The sharp edge on the rim of the orifice where the tube joins the wall represents a singularity. Peak concentrations of vorticity magnitude near the sharp edge can be as large as 15 times the wall vorticity of the undisturbed boundary layer. For this more physically realistic configuration the onset of instability occurs at smaller R.

Introduction

The jet in cross-flow refers to flow from a nozzle in a wall that interacts with the surrounding boundary layer developing on the wall. The jet in cross-flow has been subject to extensive experimental, numerical and theoretical investigations because of its practical relevance. Applications include plumes of smoke and pollutants, fuel injection and mixing or film cooling. Experimental studies include (6), (8), (12) and (4). Numerical and theoretical investigations include (2), (3), (14), (10), and (15) These represent only some of the main contributions. Mahesh (9) provides a recent review.

The parameters controlling the characteristics of the jet in cross-flow include the Reynolds numbers of the jet inflow and the cross-flow boundary layer, the shape and size of the inlet pipe for the nozzle, and the velocity ratio R, which is the most important parameter. A number of definitions of R have been used, including configurations in compressible flow which account for the fluid density of the jet and cross-flow. In this paper R is defined in the same way as (1) and (7), i.e.

$$R = \frac{V}{U_1} \tag{1}$$

where V is the maximum in inflow velocity profile of the jet and U_1 is the free-stream velocity of the cross-flow boundary layer.

DNS (Direct Numerical Simulations) of the low amplitude jet in cross-flow have recently been investigated by the group at the Dept. of Mechanics, Roy. Inst. Tech. in Sweden,(KTH). (1) used the fully spectral, massively parallel spectral DNS solver called SIMSON. For small values of R the flow is steady and consists of a counter-rotating vortex pair. As R is increased the onset of shedding of horseshoe vortices occurs at a particular value of R. With further increases in R the flow evolves into a more complicated quasi-periodic behaviour, before finally becoming turbulent. In a follow on study (7) performed a global linear stability analysis that predicts well the frequency and initial growth rate of the nonlinear DNS at the critical value of R for the onset of shedding.

The overall agreement between nonlinear DNS and the predictions from global linear stability analysis establishes the low-amplitude jet in cross-flow as a significant test case for investigating the capabilities and limitations of various CFD solvers.

The configuration studied (1) and (7) will be termed the *KTH* configuration. In this paper, the behaviour of the *KTH* configuration will be simulated using the ANSYS Fluent CFD solver. The conditions for the onset of instability, decay of transients and other characteristics in the Fluent solutions will be compared to the *KTH* results.

CFD Configuration

In the *KTH* configuration the jet inflow velocity profile is introduced on the wall as a Dirichlet boundary condition in a spatially developing Blasius boundary layer using the following simplified parabolic jet inflow profile which is multiplied by a super-Gaussian smoothing function:

$$v(r)/U_1 = R(1-r^2)\exp[-(r/0.7)^4] \tag{2}$$

where r is the distance from the centre of the jet, normalized by half the jet diameter, D. The profile is shown in figures 1(a-b).

In the *KTH* configuration the nozzle diameter, $D = 3$ and the Reynolds number based on the displacement thickness of the incoming boundary layer $Re_{\delta_0^*} = 165$. The jet nozzle centre is located at $x = 9.375\delta_0^*$ downstream of the inflow location, with boundary layer displacement thickness, $\delta^* = 1.08$, corresponding to $Re_{\delta^*} \approx 178.2$.

Corresponding results are presented here using ANSYS Fluent with a CFD mesh developed for a synthetic jet application by (13). The orifice diameter, $D = 1.0$ mm for the synthetic jet mesh leading to a corresponding unit Reynolds number, $Re_u = 495,000\ \mathrm{m}^{-1}$. For the default Fluent kinematic viscosity for air of $\nu = 1.4607\times10^{-5}\mathrm{m}^2\mathrm{s}^{-1}$ the Reynolds number scaling leads to a free-stream velocity, $U_1 = 7.230\ \mathrm{ms}^{-1}$, and the physical location of the inlet, $x_i = 0.0185$ m and the jet, $x_j = 0.02166$ m. In a physical configuration the orifice would be located close the leading edge where the cross-flow boundary layer grows relatively rapidly.

The CFD mesh developed by (13) for the synthetic jet uses the flow from an entry tube attached to the orifice to form the jet. For the *KTH* configuration, the tube is removed and the orifice inflow boundary condition is specified using equation (2). The two-dimensional axisymmetric inlet velocity profile for the jet for $R = 0.65$ is shown in figures 1(a-b) for two different mesh resolutions.

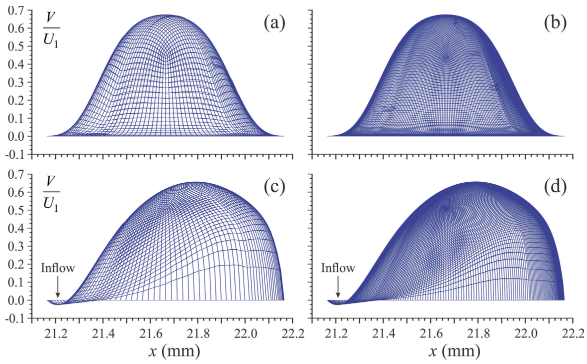

Figure 1: View from z-direction of two-dimensional profiles of the orifice jet velocity for $R = 0.65$: *KTH* configuration, (a) Coarse mesh; (b) Fine mesh; Configuration with tube, (c) Coarse mesh; (d) Fine mesh.

More physically realistic simulations are also conducted in which the length of the entry tube for the jet of length, $L = 20$ mm, i.e. $L/D = 20$. Sharp edges can introduce significant errors in viscous flow simulations. Exact solutions can be singular at sharp edges and numerical solutions can diverge in the singular region. The sharp-edge on the rim of the orifice where the tube joins the wall represents a singularity where the local solutions of vorticity become increasingly large as the mesh is further refined. Preliminary investigations showed that local concentrations of vorticity magnitude are far in excess of the vorticity in the surrounding boundary layer. This is an important consideration since the resolution of the flow in the vicinity of the orifice must be sufficient to obtain an accurate representation of the magnitude of the shear in the emerging jet, which will effect the stability of the flow downstream.

CFD Mesh

The CFD mesh consists of a base mesh which has been locally subjected to adaption, twice, in the region surrounding the jet orifice and extending downstream to the Outflow. Each adaption doubles the mesh resolution in each direction, leaving hanging nodes on the adaption boundary. Hence the finer mesh surrounding and downstream of the jet orifice is 64 times more dense per unit volume than the surrounding base mesh, i.e. $(2^3)^3$. The motivation is that the resolution of the base mesh need only be sufficient to properly resolve development of the Blasius boundary layer while the much better resolution of the double-adapted mesh will be sufficient to resolve any fine-scale vortical structures downstream of the orifice. Double-adapted mesh are visible on the Wall and Outflow in figure 2.

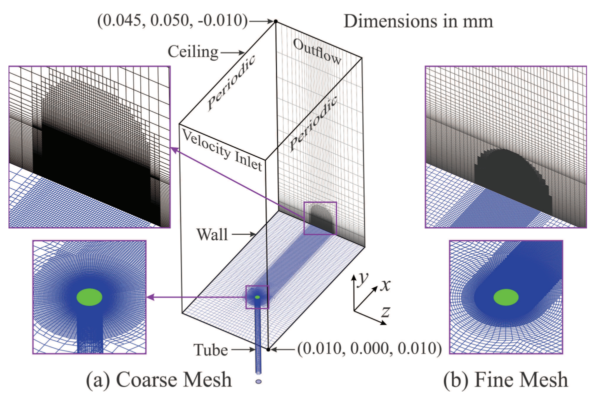

Figure 2: (a) CFD geometry: Rectangular hexahedron and 1 mm diameter tube. Coarse Mesh with close-up: 6.55M nodes. (b) Corresponding close-up of refined Fine Mesh: 34.15M nodes.

Two structured CFD meshes have been used. The geometry used for both meshes and features of the Coarse Mesh are shown in figure 2(a). The relative size and shape of the regions used for double adaption of the Coarse Mesh are much the same as for the synthetic jet study. Corresponding features of the Fine Mesh are shown in figure 2(b). A refined version of the double-adapted region has also been used for the Fine Mesh, with less extent from the wall. The refinement was was guided by the formation of vortex loops in other versions of the mesh. For all mesh the boundary of double-adapted regions occurs well away from the region containing vortex loops.

The mesh spacing in the $x-$ and $z-$directions become uniform by about five diameters downstream of the center of the orifice and the mesh resolutions in the double-adapted regions are shown in table 1. The subscript 'v' refers to use of the viscous length-scale $\sqrt{(\nu x)/U_1}$ for non-dimensional quantities. The '$+$' superscript refers to the usual turbulent viscous scaling, where ν/u_τ is used for non-dimensional quantities, where $u_\tau = \sqrt{\tau_0/\rho}$ and τ_0 is the shear stress at the wall. The Blasius boundary layer value of τ_0 at a location $5d$ downstream of the orifice is used to calculate u_τ for non-dimensional quantities. The Blasius skin friction coefficient $5D$ downstream of the orifice is given by $C_f = 6.0 \times 10^{-3}$, which is larger than the maximum C_f in a turbulent boundary layer and therefore it provides a conservative scaling. The corresponding value of the minimum grid spacing in the wall-normal direction is $y^+{}_{\min} = 0.33$ for the Coarse Mesh, and $y^+{}_{\min} = 0.14$ for the Fine Mesh. The resolution of the Fine Mesh is less than half the resolution used in the recent transition simulations reported by (11) in which $\Delta x^+ = 10$, $\Delta z^+ = 5$ and $y^+{}_{\min} = 0.4$.

	Mesh spacing					
Mesh	Δx (μm)	Δz (μm)	Δx_v	Δz_v	Δx^+	Δz^+
Coarse	106	91	0.47	0.41	2.88	2.47
Fine	43	37	0.19	0.17	1.17	1.00

Table 1: Resolution of uniform mesh in the double–adapted regions more than $5d$ downstream of the center of the orifice.

Both meshes use a fine resolution in the tube near the orifice. For the Coarse Mesh: $\delta y \approx 6.0\ \mu\text{m} \approx 1/166\ d$; and for the Fine Mesh: $\delta y \approx 4.5\ \mu\text{m} \approx 1/222\ d$. The resolution is evident in the steep gradient in the velocity profiles shown in figure 1(c-d).

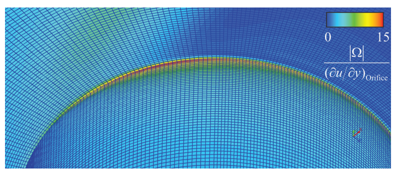

Figure 3: Sharp-edge singularity. Vorticity magnitude contours in vicinity of orifice nonondimensionalized by velocity gradient at wall of undisturbed boundary layer at $x = x_j$, and superimposed on tube and wall mesh. Fine Mesh with $R = 0.65$.

Boundary Conditions

The inflow boundary condition [Velocity Inlet in figure 2(a)] is specified by writing a profile consisting of the u and v velocity components. The velocities are replaced with corresponding Blasius values which are calculated independently using the profile coordinates. The updated Blasius profile for u and v is reloaded by the solver and spanwise velocity set to zero, $w = 0$. The ceiling is parallel to the wall and it is set as a velocity inlet with $u = U_1$, normal component set to the asymptotic transverse

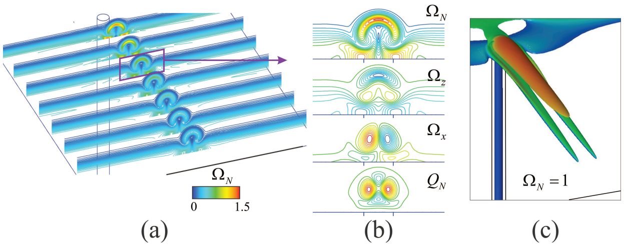

Figure 4: Steady flow, Fine Mesh with tube, $R = 0.65$. (a) Line contours of $\Omega_N = |\Omega|/(\partial u/\partial y_{\text{Orifice}})$ in spanwise planes, $\Delta x = 3, 6 \ldots 21D$ from centre of orifice. (b) Line contours, $\Omega_N(0 \to 1.5)$, $\Omega_z(\pm 1.5)$, $\Omega_x(\pm 0.3)$ and $Q_N(\pm 0.02)$ (c) Iso-surface, $\Omega_N = 1.0$: shading (blue) $-0.1 < u/U_1 < 1$ (red).

Blasius velocity, $v = 0.8604\sqrt{\nu U_1/x}$, and $w = 0$. The two side walls are set as periodic boundary conditions.

For the *KTH* configuration, the tube is removed and the orifice inflow is set as a velocity inlet with the boundary condition specified by equation (2). The axisymmetric inlet velocity profile for the jet for $R = 0.65$ is shown in figures 1(a-b) for the two different mesh resolutions. For the more realistic configuration, a uniform flow is applied to the inlet of the tube. Fully developed Poiseuille flow (with a parabolic velocity profile) was found to form after a development length, $L/D \approx 10$ for the largest tube Re. The development length is consistent with the findings of (5). The peak velocity of the parabolic profile for fully-developed Poiseuille flow, $V_{\max}$ is used to define R in equation (2), i.e. $R = V_{\max}/U_1$, where $V_{\max}$ is twice the magnitude of the uniform inlet flow. Setting the magnitude of the uniform inflow for the tube provides a convenient method for setting R for this configuration since the jet profile is significantly altered at the orifice. The resulting two-dimensional jet inlet velocity is not axisymmetric, but the peak value is close to the peak value of the symmetric profile used in the *KTH* configuration, as shown in figure 1(c-d) for two different mesh resolutions for $R = 0.65$.

CFD Method

Unsteady time series are generated from the corresponding steady solution for each R. The steady solutions use the pressure-based, coupled solver with second-order upwind differencing for pressure and third-order MUSCL discretization scheme for momentum. The steady solutions typically required more than 20,000 iterations for global continuity residual convergence to 1×10^{-8}.

For the unsteady time series the steady solution is loaded and the general model changed to a pressure-based transient solver. Non-Iterative Time Advancement (NITA) was found to be significantly faster than iterative schemes. Second-order fractional-step is used for the pressure-velocity coupling, with second-order for the pressure.

Numerical noise provides the background disturbance for exciting the instabilities It is important to minimize the numerical dissipation and to avoid damping of the smallest scales. Central Differencing was used since it is the least dissipative and provides the highest resolution accuracy for smallest scales. Resolution is checked by comparing results using the different mesh.

Results

Contours of vorticity magnitude for the Fine Mesh with $R = 0.65$ are shown figure 3. As mentioned earlier, the sharp-edge

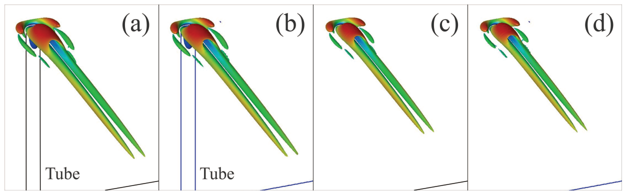

Figure 5: Steady flow, $R = 0.65$. Iso-surfaces of $Q_N = 0.002$: second invariant of the velocity gradient tensor Q nondimensionalized by $(\partial u/\partial y_{\text{Orifice}})^2$, shading (blue) $-0.1 < u/U_1 < 1$ (red). Configuration with tube: (a) Fine Mesh (b) Coarse Mesh. *KTH* configuration: (c) Fine Mesh (d) Coarse Mesh.

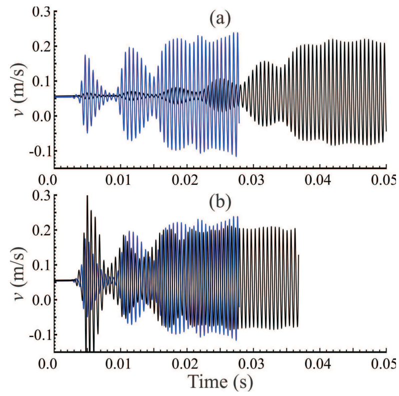

Figure 6: Time histories for *KTH* configuration, $R = 0.65$, using probe shown in figure 7. (a) Coarse Mesh. Central differencing (blue), Upwind differencing (black). (b) Central differencing. Coarse Mesh (blue), Fine Mesh (black).

on the rim of the orifice where the tube joins the wall represents a singularity where the local solutions of vorticity becomes increasingly large as the mesh is further refined. Most of the wall vorticity of the layer is accounted for by $\partial u/\partial y_{\text{Orifice}}$. The peak vorticity near the rim of the orifice occurs off-centerline and it is approximately 15 times greater than the vorticity in the surrounding boundary layer. Proper resolution of the local concentration of vorticity is an important consideration since the flow in the vicinity of the rim will form the shear in the emerging jet. The shear on the jet boundary will effect the stability characteristics of the counter-rotating vortex pair and the onset of the formation of horseshoe vortices downstream.

Figure 4(a) shows the development of vorticity Ω_N in cross-stream planes downstream of the orifice for the configuration with the tube for $R = 0.65$. The main features are the counter-rotating vortex pair, which consist mainly of streamwise vorticity, ω_x, and the head of the loop, which consists mainly of spanwise vorticity, ω_z, as shown in the larger-scale views of $\Omega_x = \omega_x/(\partial u/\partial y_{\text{Orifice}})$ and $\Omega_z = \omega_z/(\partial u/\partial y_{\text{Orifice}})$ in figure 4(b). The vorticity development is also apparent in the iso-surface $\Omega_N = 1.0$ in figure 4(c) which is shaded using the local streamwise velocity.

The second invariant of the velocity gradient tensor, Q, is often used to identify Λ-vortices in transitional and turbulent boundary layers, e.g. Sayadi et al. (11). Line contours of Q_N (defined in figure 5 caption) show a marked similarity with contours of Ω_x. Bagheri et al. (1) and Ilak et al. (7) used this technique to identify vortex loops in the *KTH* simulations.

Horseshoe vortices for $R = 0.65$, are clearly seen in the results for the *KTH* configuration in figure 7. Corresponding results for the case with the tube are shown in figure 8. Here the horseshoe vortices are larger and more energetic. Horseshoe vortices for $R = 0.60$ for the case with the tube are shown in figure 9. The horseshoes do not form for this R in the *KTH* configuration

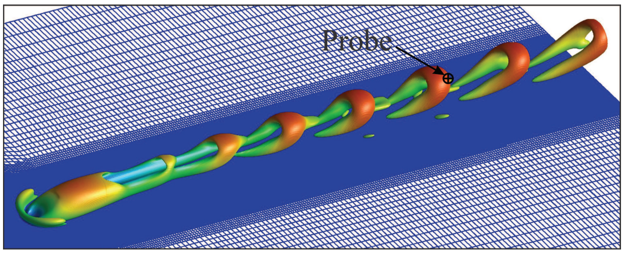

Figure 7: Horseshoe vortices, *KTH* config., $R = 0.65$, original Fine Mesh. Iso-surface, $Q_N = 0.01$, shading: (blue) $-0.1 < u/U_1 < 1.1$ (red). Probe location shown for time histories.

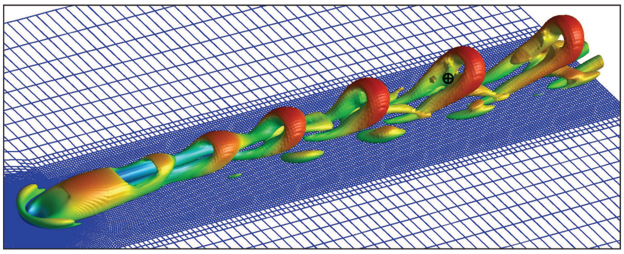

Figure 8: Horseshoe vortices, with tube, $R = 0.65$, Coarse Mesh. Iso-surface, $Q_N = 0.01$, shading as in figure 7.

(without the tube). The time histories in figure 10 show a much reduced magnitude v fluctuation. The cause of the substantial modulation in v seen by the probe originates from an overall modulation in the formation of the horseshoe vortices. The reason for the modulation in horseshoe formation is unknown at this stage.

Conclusions

Results with much the same stability characteristics have been obtained using the ANSYS Fluent CFD solver corresponding to the *KTH* configuration. Simulations in which the jet fluid originates from a tube connected to wall show peak concentrations of vorticity near the sharp edge of the orifice which can be as large as 15 times the wall vorticity of the undisturbed boundary layer. For this more physically realistic configuration the onset of instability occurs at smaller value, $R = 0.60$.

Acknowledgements

The computations were performed on the Trifid HPC cluster provided by the V3 Alliance and the assistance of the RMIT eResearch Office is gratefully acknowledged.

*

References

[1] Bagheri, S., Schlatter, P., Schmid, P. J. and Henningson, D. S., Global stability of a jet in crossflow, *J. Fluid Mech.*, **624**, 2009, 33–44.

[2] Coelho, S. L. V. and Hunt, J. C. R., The dynamics of the near field of strong jets in crossflows, *J. Fluid Mech.*, **200**, 1989, 95–120.

[3] Cortelezzi, L. and Karagozian, A. R., On the formation of the counter-rotating vortex pair in transverse jets, *J. Fluid Mech.*, **446**, 2001, 347–373.

[4] Davitian, J., Getsinger, D., Hendrickson, C. and Karagozian, A. R., Transition to global instability in transverse-jet shear layers, *J. Fluid Mech.*, **661**, 2010, 294–315.

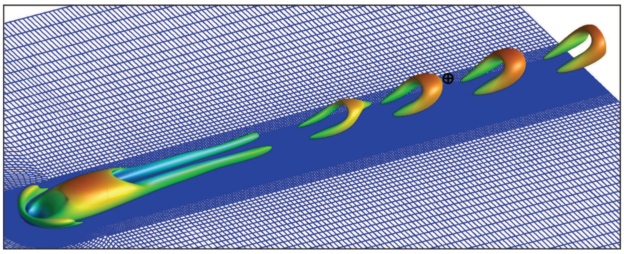

Figure 9: Horseshoe vortices, with tube, $R = 0.60$, revised Fine Mesh. Iso-surface, $Q_N = 0.01$, shading as in figure 7.

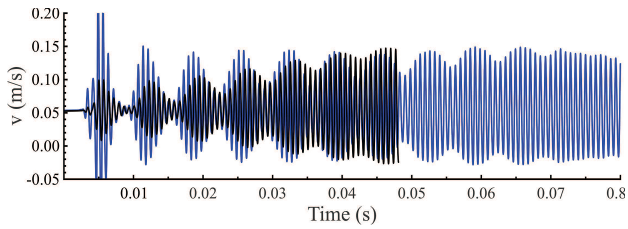

Figure 10: Time histories for configuration with tube, $R = 0.60$. Probe location as per figure 7. Central differencing: Coarse Mesh (blue), Fine Mesh (black).

[5] Durst, F., Ray, S.and Unsal, B. and Bayoumi, O. A., The development lengths of laminar pipe and channel flows, *J. Fluids Eng.*, **127**, 2005, 1154–1160.

[6] Fric, T. F. and Roshko, A., Vortical structure in the wake of a transverse jet, *J. Fluid Mech.*, **279**, 1994, 1–47.

[7] Ilak, M., Schlatter, P., Bagheri, S. and Henningson, D. S., Bifurcation and stability analysis of a jet in cross-flow: onset of global instability at a low velocity ratio, *J. Fluid Mech.*, **696**, 2012, 94–121.

[8] Kelso, R. M., Lim, T. T. and Perry, A. E., An experimental study of round jets in cross-flow, *J. Fluid Mech.*, **306**, 1996, 111–144.

[9] Mahesh, K., The interaction of jets with crossflow, *Annual Rev. Fluid Mech.*, **45**, 2013, 379–407.

[10] Muppidi, S. and Mahesh, K., Study of trajectories of jets in crossflow using direct numerical simulations, *J. Fluid Mech.*, **530**, 2005, 81–100.

[11] Sayadi, T., Hamman, C. W. and Moin, P., Direct numerical simulation of complete h-type and k-type transitions with implications for the dynamics of turbulent boundary layers, *J. Fluid Mech.*, **724**, 2013, 480–509.

[12] Smith, S. H. and Mungal, M. G., Mixing, structure and scaling of the jet in crossflow, *J. Fluid Mech.*, **357**, 1998, 83–122.

[13] Watmuff, J., Combined numerical and experimental investigation of instability and breakdown of a synthetic jet, *AIAA Paper AIAA-2011-3567. 41st AIAA Fluid Dynamics Conference and Exhibit, June 27-30, 2011, Honolulu, Hawaii.*.

[14] Yuan, L. L., Street, R. L. and Ferziger, J. H., Large-eddy simulations of a round jet in crossflow, *J. Fluid Mech.*, **379**, 1999, 71–104.

[15] Ziefle, J. and Kleiser, L., Large-eddy simulation of a round jet in crossflow, *AIAA J.*, **47**, 2009, 1158–1172.